$HfCo_2$ Laves phase intermetallics—part I: solubility limits and defect mechanisms

Katherine C. Chen*, Eric J. Peterson, Dan J. Thoma

Materials Science and Technology Division, Los Alamos National Laboratory, Los Alamos, NM 87545, USA

Abstract

Solubility limits and constitutional defects in Laves phase intermetallics are investigated with the *C*15 $HfCo_2$ system. Several binary alloy compositions based on $HfCo_2$ are characterized by optical and scanning electron microscopy (SEM), electron microprobe analysis (EPMA), X-ray diffraction (XRD), and density measurements. Rietveld refinements of XRD scans are used to determine lattice constants, anisotropic strain parameters, and atomic occupancies. Compositional trends are compared against predicted or calculated trends due to an anti-site substitution or vacancy defect mechanism. Geometric models and atomic size factors are used to establish solubility limits and to give insight into defect mechanisms. Results from various, complementary experiments are consistent with anti-site substitutions on both sides of $HfCo_2$ stoichiometry.

Keywords: A. Intermetallics, miscellaneous; A. Laves phases

1. Introduction

The development of Laves phase intermetallics for potential engineering applications, such as high-temperature structural materials [1], giant magnetostrictives [2], and hydrogen storage [3], requires the fundamental understanding of structure-property relationships. Since constitutional defects can profoundly affect properties, the defect mechanism must first be established. Therefore, this study thoroughly investigates the $HfCo_2$ system in order to understand defect mechanisms in the class of Laves phase intermetallics. Furthermore, understanding of the effects of constitutional defects enables the development of alloying strategies for optimized properties.

Although most binary Laves phases (AB_2) are observed to be "line compounds", several systems exhibit solubility ranges. The ability of a Laves phase to accommodate nonstoichiometry can be related to the atomic size requirements for a topologically close-packed structure and to lattice-adjusted contractions [4]. Based upon a hard-sphere model, Laves phases with a metallic radius ratio (R_A/R_B) close to the ideal value of 1.225 are found to exhibit a range of homogeneity [4]. The $HfCo_2$ Laves system has a radius ratio close to the ideal ($R_{Hf}/R_{Co} = 1.26$), and the current equilibrium phase diagram shows a relatively large homogeneity range of 9 at.% (Fig. 1) [5].

Although the single-phase fields of $TiCr_2$ [6] and $NbCr_2$ [7–9] have been studied in detail, these particular Laves phases have a radius ratio (R_A/R_B) less than 1.225, and a larger solubility range on the A-rich sides of the AB_2 stoichiometry. $HfCo_2$, on the other hand, has greater solubility on the B-rich side of stoichiometry, and is more representative of Laves phases in general. Thus, the large solubility range (especially towards the B-rich side) of $HfCo_2$ provides a more complete and comprehensive opportunity to study the solubility limits and defect mechanisms of Laves phase intermetallics. In addition, the almost-ideal size ratio of $HfCo_2$ substantiates the use of hard sphere models to interpret the results. No previous study on a Laves phase has investigated solubility ranges and defect mechanisms with the combination of geometrical size principles and several different experimental techniques.

* Corresponding author now at: Materials Engineering Department, California Polytechnic State University, San Luis Obispo, CA 93407, USA.

E-mail address: kcchen@calpoly.edu (K.C. Chen).

Lattice constants and densities have been measured as a function of composition, and have been used to assert anti-site substitutions in several Laves phase systems, such as $NbCr_2$, $ZrCo_2$ [10] $NbCo_2$ [11,12], $NbFe_2$ [13], $TiFe_2$ [14], $TiMn_2$ [15], and $ZrMn_2$ [16]. However, not all Laves phases have been reported to accommodate solely anti-site substitutions. Vacancies were proposed on the B-rich side and anti-sites on the A-rich side of stoichiometry in $NbCr_2$ [7] and YAl_2 [17]. Thus, the generalization of defect mechanisms in Laves phases cannot be made without further qualifications. Several different and new approaches are taken in this study of $HfCo_2$. Each result is analyzed to contribute to a consistent conclusion.

Once the defect mechanism is identified, deformation and properties of Laves phases can be better understood, and even manipulated. For instance, the accepted deformation mechanism of Laves phases, "synchroshear", involves the coordinated motion of successive atomic layers, and any deviation from a perfect lattice alters the process [18]. In turn, mechanical properties are affected. The hardness of intermetallics is well documented to be dependent upon the composition and is related to dislocation interactions with defects [19]. Hence, alloying strategies entail achieving the correct structure for the desired property. The effect of constitutional defects on the elastic and mechanical properties of $HfCo_2$ is the subject of Part II of this paper [20].

2. Experimental procedures

Nine different alloy compositions spanning the *C*15 $HfCo_2$ Laves phase field were prepared using Co (99.995%) and Hf (99.9+%). The selected nominal compositions can be found in Table 1. The alloys were arc-melted, flipped, and remelted several times to ensure homogeneity. Heat treatments were performed at 1200 °C for 100 h, followed by 1400 °C for 100 h, and slow cooled. Chemical analysis of a heat-treated sample by inert gas fusion revealed impurity levels of 0.044 wt.% oxygen and 0.058 wt.% nitrogen.

Compositions of the heat-treated alloys were determined by electron probe microanalysis (EPMA). A large area analysis was performed in order to determine the bulk alloy composition of each sample, as well as, analyses of different phases within the alloys. The different phases were also identified by X-ray diffraction (XRD) using a Scintag XDS 2000 with a Cu K_α radiation source. Powder samples with an internal Si standard reference material (NBS 640b) were scanned over a 2θ range of 20–135°. The Rietveld refinement method [21] was then utilized to determine the lattice constants, using the program (GSAS Generalized Structural Analysis System) [22]. Rietveld refinements were also carried out to determine strain parameters and atomic site occupancies. For the strain parameter study, powder samples were also annealed at 800 °C to examine the effects of powder preparation. A detailed report on the procedures and analysis of these refinements is the subject of another paper [23], and only the main results are discussed here.

For modeling efforts, two different defect mechanisms were considered for each alloy sample composition. The atomic contents of 100 sites (33 A sites and 67 B sites) were generated to match each alloy composition with either only anti-site substitutions or only vacancies (Table 2). These atomic occupancies were used for the XRD simulations and calculated densities. Ca.R.Ine Crystallography software was used to model the crystalline structure of each alloy with the appropriate composition and defect mechanism. Experimentally determined lattice constants for each sample were used in the simulations such that the XRD peaks would occur at the same 2θ positions. Thus, the intensities would be primarily dependent upon the different atomic contents of the unit cell (through the structure factor), and comparisons between the two defect mechanisms could be compared. The simulated intensities accounted for the Lorentz factor, polarization factor, temperature

Table 1
Nominal alloy compositions, heat treated bulk compositions, and Laves phase compositions determined by electron microprobe analysis. Phases in each alloy sample found by X-ray diffraction (XRD) and metallography

	Nominal	bulk alloy composition			Laves phase composition			Phases
#	(at.% Co)	(at.% Co)	(at.% Hf)	(at.% Zr)	(at.% Co)	(at.% Hf)	(at.% Zr)	
4	64.0	61.70±0.62	36.20±0.58	2.17±0.12	64.70±0.23	33.20±0.21	2.14±0.06	HfCo + $HfCo_2$
3	65.0	63.00±0.42	34.80±0.36	2.19±0.15	65.20±0.23	32.80±0.17	2.07±0.07	HfCo + $HfCo_2$
2	66.0	64.00±0.32	34.00±0.32	2.04±0.09	65.50±0.06	32.50±0.08	2.02±0.06	HfCo + $HfCo_2$
1	67.0	64.60±0.02	33.20±0.21	2.13±0.10	65.50	32.50	1.96	HfCo + $HfCo_2$
5	68.0	66.30±0.23	31.80±0.25	1.95±0.14	66.10±0.31	31.90±0.34	1.98±0.06	$HfCo_2$
6	70.0	67.30±0.32	30.90±0.28	1.83±0.08	67.40±0.22	30.70±0.21	1.89±0.05	$HfCo_2$
7	71.0	69.00±0.35	29.20±0.38	1.73±0.11	69.37±0.13	28.86±0.15	1.77±0.07	$HfCo_2$
8	72.0	70.50±0.26	27.70±0.26	1.79±0.07	70.60±0.09	27.60±0.10	1.77±0.07	$HfCo_2$
9	73.0				72.03±0.15	26.29±0.14	1.68±0.07	$HfCo_2$

Table 2
The atomic constituents per 100 Laves phase sites (33 A sites and 67 B sites) for each alloy sample (as given by microprobe analysis) with entirely anti-site substitutions or with entirely vacancies as the defect mechanism. Note the first two samples are Hf-rich and the rest are Co-rich

Microprobe			Anti-site substitutions						Vacancies					
composition			A sublattice			B sublattice			A sublattice			B sublattice		
Co	Hf	Zr	Co	Hf	Zr	Co	Hf	Zr	Co	Hf	Zr	Co	Hf	Zr
65.5	32.5	2.0	0	31.4	1.9	65.5	1.1	0.1	0	31.4	1.9	63.4	0	0
66.1	31.9	2.0	0	31.3	2.0	66.1	0.6	0	0	31.3	2.0	65.0	0	0
67.4	30.7	1.9	0.7	30.7	1.9	66.7	0	0	0	30.4	1.9	66.7	0	0
69.4	28.8	1.8	2.7	28.8	1.8	66.7	0	0	0	27.7	1.7	66.7	0	0
70.6	27.6	1.8	3.9	27.6	1.8	66.7	0	0	0	26.1	1.7	66.7	0	0
72.0	26.3	1.7	5.3	26.3	1.7	66.7	0	0	0	24.3	1.6	66.7	0	0

factor, and the multiplicity factor. The peak intensity (I) for each hkl plane was computed by the equation:

$$I_{hkl} = |F_{hkl}|^2 \left(\frac{1 + \cos^2 2\theta}{\sin^2 \theta \cos \theta} \right) e^{-2B\left(\frac{\sin\theta}{\lambda}\right)^2} p \quad (1)$$

where θ is the Bragg angle, F is the structure factor, B is a quantity dependent on the amplitude of thermal vibration and scattering angle, p is the multiplicity factor, and λ is the radiation wavelength.

Experimental densities were determined by water immersion, using Archimedes principle [24]. Calculated densities (ρ) of alloy compositions with anti-sites or with vacancies (i.e. missing atoms) were computed by:

$$\rho = \sum_i \frac{(C_i M_i) N_c}{N_0 V} \quad (2)$$

where C_i = number of atoms of type i in the unit cell, M_i = mass per mole of atoms of type i, N_c = number of atoms per unit cell, N_o = Avogadro's number, and V = volume of unit cell. Experimental lattice constants were used to compute the volume. Thus, given an alloy composition and volume, different atom contents (corresponding to different defect mechanisms) will produce different density values.

3. Results

3.1. Microstructures and phases

Results from XRD confirm that the $HfCo_2$ Laves phase in all the alloys has the cubic $C15$ crystal structure. The Hf-rich alloys (samples #1–4) contain two phases, HfCo ($B2$) and $HfCo_2$. Table 1 lists the nominal compositions and heat treated bulk alloy compositions determined by microprobe analysis (EPMA). Comparisons show that Co was consistently lost during the processing of the alloys. In addition, Zr appears in all the alloys and is unavoidable, due to the commercial Hf source. The Zr is treated as a substitute for Hf, and appears to partition equally to the HfCo and $HfCo_2$ phases. Small amounts of Hf-rich nitrides and oxides are also detected in all the alloys by EPMA and XRD.

Table 1 also lists the compositions of the $C15$ $HfCo_2$ Laves phase, and delineates the single-phase field. The composition range at 1400C extends from approximately 65.0 at.% Co to at least 72.0 at.% Co. The reported lower Co-content of the Laves phase of samples #3 and #4 in Table 1 is believed to result from probing parts of the second phase, HfCo, in the measurements, and therefore are not accurate values for $HfCo_2$. Furthermore, lattice constants are more accurate and sensitive measurements for the solubility limit, and are discussed later. The Laves phase field from this study is slightly different from that of the current phase diagram (Fig. 1 [5]), which reports a range of 64–73 at.% Co.

Fig. 2a and b are optical micrographs of the as-cast microstructures of the Hf-61.7 at.% Co (sample #4) and Hf-64.6 at.% Co (sample #1) alloys, respectively. Coarse $HfCo_2$ dendrites can be seen, and the interdendritic regions exhibit eutectic structures. The heat-treated microstructures of the same two alloy samples are shown respectively in Fig. 2c and d. The eutectic structure no longer exists after the long annealing times. However, remnants of the dendritic microstructure are still evident in the low-magnification SEM image of the Hf-63.0 Co alloy in Fig. 3. Alloy samples of 66.3–71.9 at.% Co (samples #5–9) were essentially single-phase $C15$. Tiny Hf-rich nitride dendrites and spherical oxide pullouts are depicted in Fig. 4. These impurities are found dispersed throughout all of the alloys.

3.2. X-ray diffraction analysis

Fig. 5 displays the $HfCo_2$ $C15$ lattice constant as a function of the Hf-Co (bulk) alloy composition of the heat-treated samples. The error in the lattice constant (± 0.00015 Å) is smaller than the data point marker in the plot. For bulk alloy compositions 61.7–65.0 at.% Co, a constant $C15$ lattice constant of 6.919 Å results. These Hf-rich alloys (samples #1–4) correspond to the equilibrium two-phase field of HfCo + $HfCo_2$. Within the two-phase region, the alloys contain the same two phases as dictated by a tie-line on the phase diagram (and the amounts of each phase differ according to the lever rule). The same Hf-rich Laves composition (i.e. Hf–65 Co) appears in all these samples and thus has the same lattice constant. However, within the single-phase field (samples #5–9), a decrease in lattice constant occurs with an increase in Co-content. A linear relation

between the Laves phase composition (x, in at.% Co) and unit cell size (a) is as follows:

$$a = 7.6409 - 0.011107x \quad (3)$$

Broadening of XRD peaks due to non-uniform strain is analyzed with Rietveld refinements, and the results are plotted in Fig. 6. The anisotropic strain parameters are separated into two components: parallel to [111] and perpendicular to [111], the direction of the stacking of close-packed planes in the $C15$ Laves structure. The strain ∥ [111] reveals a maximum near the stoichiometric composition, while the strain ⊥ [111] (or within the close-packed plane) displays a minimum near stoichiometry. Increasing off-stoichiometry in both the Hf-rich and Co-rich directions result in larger anisotropy in the strain parameter, and the stoichiometric composition appears to be fairly isotropic. The strain associated with the heat treated powders appears to be slightly lower than the unannealed powder samples. The most significant change occurs with the most Hf-rich composition.

3.3. XRD simulations and Rietveld-refined occupancies with defect models

For each nonstoichiometric alloy, the two extreme defect mechanisms (anti-sites vs. vacancies) result in different atomic occupancies on each sublattice. These atomic occupancies (Table 2) are used to simulate XRD patterns for each alloy sample. The simulated XRD intensities from the two defect mechanisms are compared against the experimental scans. Mixed or complex defect structures are not considered in this study, and remain a possibility. From Eq. (1), the intensities of each *hkl* peak depend primarily on the structure factor, F. All other factors should remain constant for each composition since the lattice constant (and thus θ) are the same. Table 3 lists the structure factors for *hkl* planes in the $C15$ Laves phase. Differences in the atomic constituents result in differences in XRD intensities [25]. For example in Co-rich compositions, either excess Co atoms occupy the A-sublattice sites (via anti-site substitutions), or Hf vacancies occur on the A-sublattice. Both cases result in a decrease in the atomic scattering

Table 3
Structure factors for the $C15$ Laves phase. The (222) plane depends only on the B sublattice, and thus should stay constant for the Co-rich $HfCo_2$ Laves phases

hkl	F^2_{hkl}
111	$2(4f_A - 5.656f_B)^2$
220	$(8f_A)^2$
311	$2(4f_A + 5.656f_B)^2$
222	$(16f_B)^2$
331	$2(4f_A - 5.656f_B)^2$
422	$(8f_A)^2$
333/511	$2(4f_A + 5.656f_B)^2$
440	$(8f_A + 16f_B)^2$
531	$2(4f_A - 5.656f_B)^2$

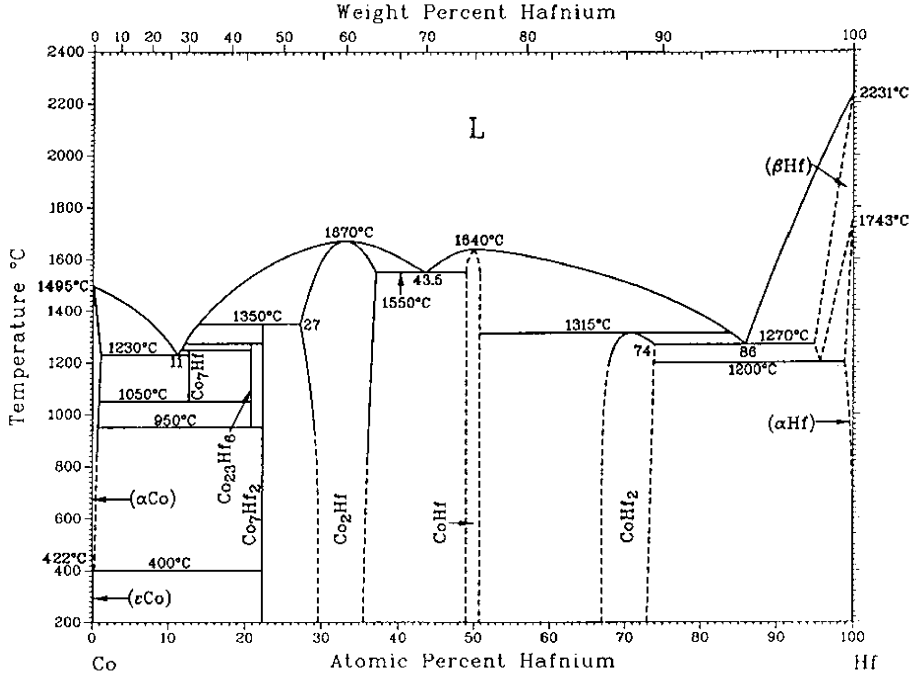

Fig. 1. The current Hf-Co equilibrium phase diagram [5].

factor of the A-sublattice, f_A, but to different extents. The lack of an atom (i.e. a vacancy) essentially represents an atomic scattering factor of zero, and thus reduces the structure factor considerably.

The structure factor for the (222) plane, however, depends only on f_B. Any changes to the A sublattice should not affect the (222) peak intensity, and this peak intensity should be constant for all the Co-rich alloys.

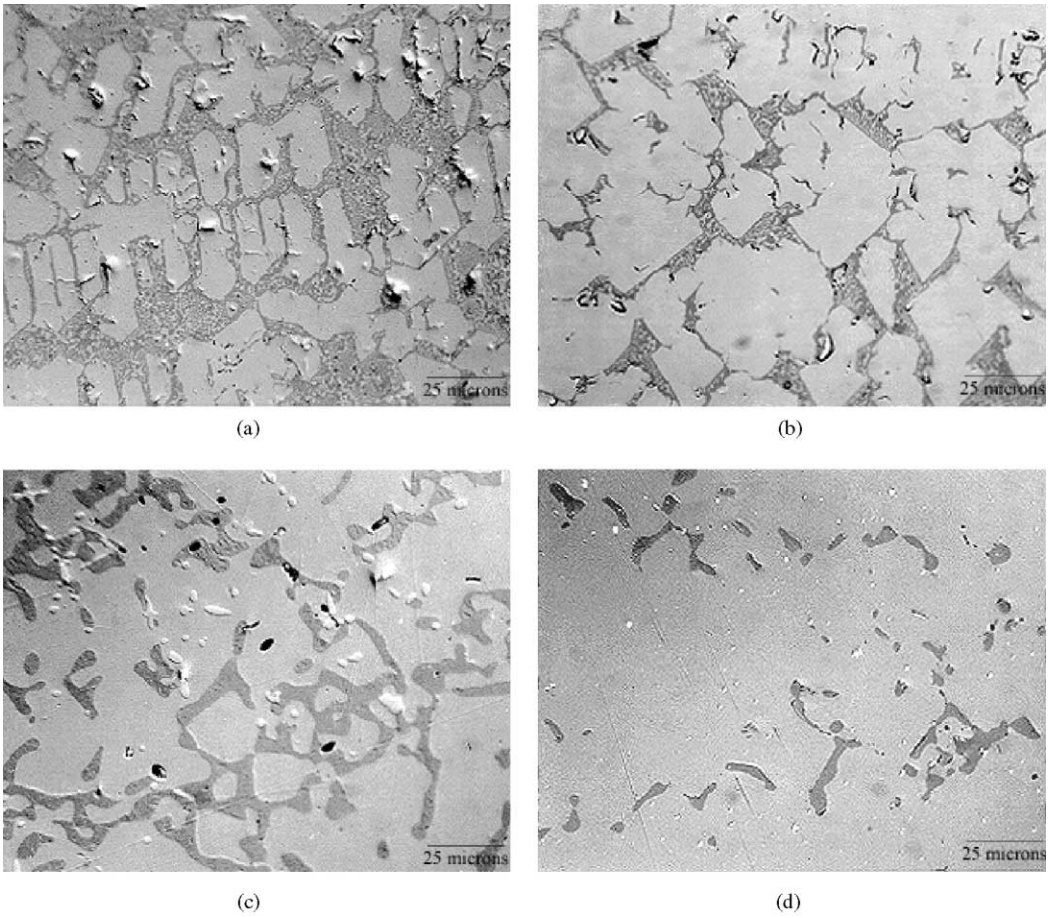

Fig. 2. Optical micrographs of the (a) as-cast Hf-61.7 Co, (b) as-cast 64.6 Co, (c) heat-treated Hf-61.7 Co, and (d) heat-treated Hf–64.6 Co alloy.

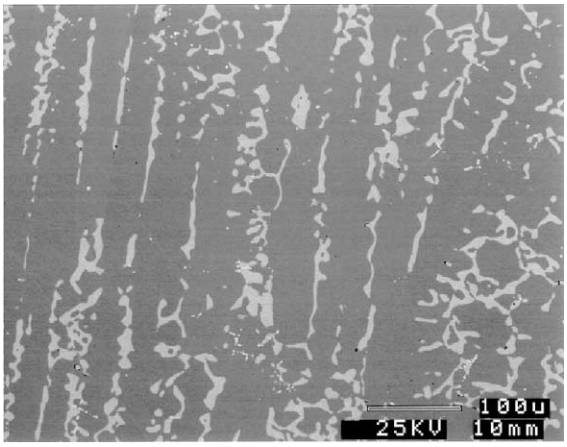

Fig. 3. SEM image of the remnant dendritic microstructure in the heat-treated Hf-63.0 Co alloy.

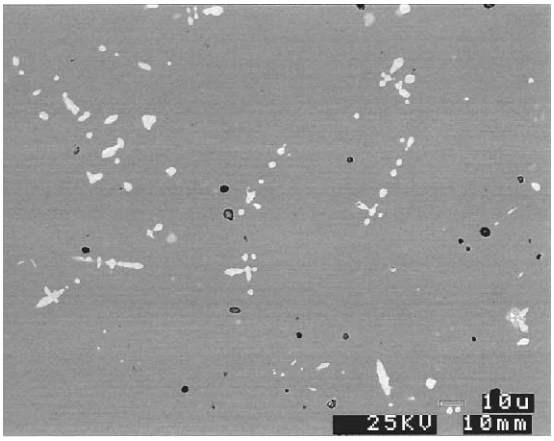

Fig. 4. Small nitride dendrites (light contrast) and spherical oxide pullouts (dark contrast) are found throughout the alloy samples.

Thus, all peak intensities for the Co-rich compositions are normalized to the (222) intensity. In addition, the peak intensities are also analyzed relative to the alloy closest to stoichiometry (#6, Hf-67.4 Co), in order to remove any instrument biases. Fig. 7 displays the results for the most Co-rich alloy (#9, Hf-71.9 Co). Comparisons of the experimental to simulated intensities suggest that the anti-site substitution mechanism is operative

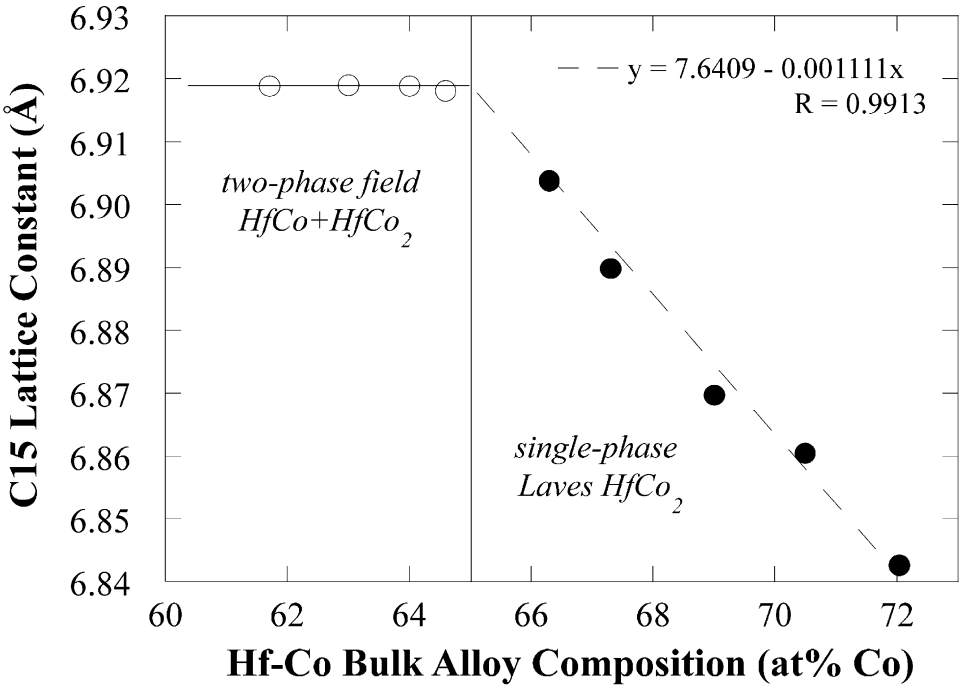

Fig. 5. The *C*15 lattice constant versus the bulk Hf-Co alloy composition. The two-phase field is distinguished by the fixed lattice constant from 61.7 to 65.6 at% Co. A nearly linear relationship occurs within the single phase Laves region.

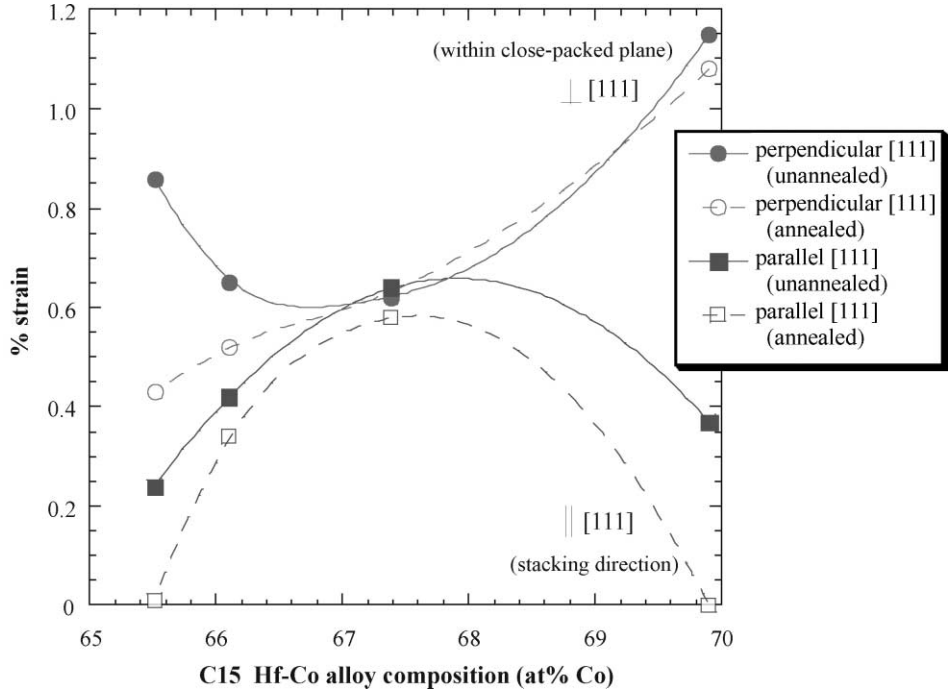

Fig. 6. Anisotropic strain parameters as a function of $HfCo_2$ Laves phase composition. The average strain parallel to [111] is essentially constant. However, the strain perpendicular to [111] displays a minimum around the $HfCo_2$ stoichiometry.

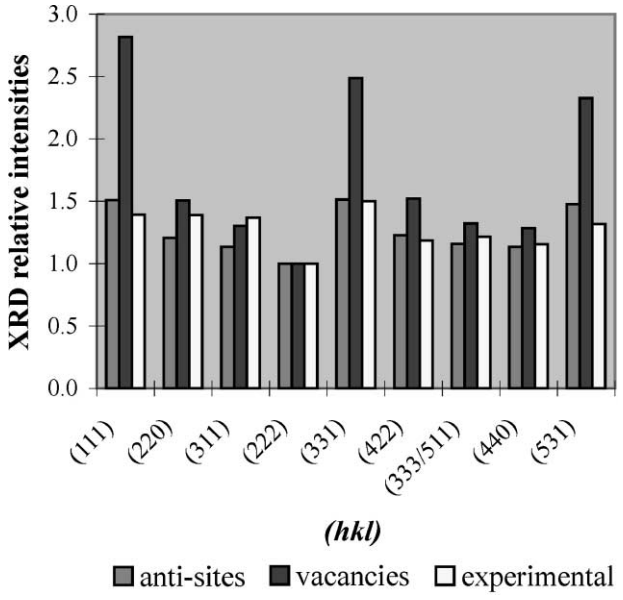

Fig. 7. Simulated intensities of the Hf-72.0 Co alloy with anti-site substitutions and with vacancies are compared against experimental results. (The XRD intensities are normalized to the 222 plane and relative to the stoichiometric alloy.)

for the Co-rich side of stoichiometry. The other Co-rich samples demonstrate similar trends. Analysis of the Hf-rich side are more difficult (owing to the smaller solubility range and smaller intensity differences for comparisons), and thus, are inconclusive by this particular method.

As with the XRD simulations, Rietveld refinements on the alloy compositions depend only on the contents of each sublattice. Rietveld refinements use the experimental XRD intensities to refine the atomic occupancies of the separate A and B sublattices of the AB_2 Laves phase. Allowing only anti-site substitutions or only vacancies on particular sublattices, atomic occupancies are generated that are consistent with the XRD intensities. The resulting compositions are then compared against microprobe compositions to determine the soundness of the different defect mechanisms (i.e. anti-sites or vacancies). A perfect fit is represented by a one to one correspondence in the EPMA to Rietveld-refined compositions, and thus a straight line of slope = 1 is drawn in Fig. 8.

For the Co-rich $HfCo_2$ alloys, the plot reveals that the trend of the Rietveld refined compositions with Co

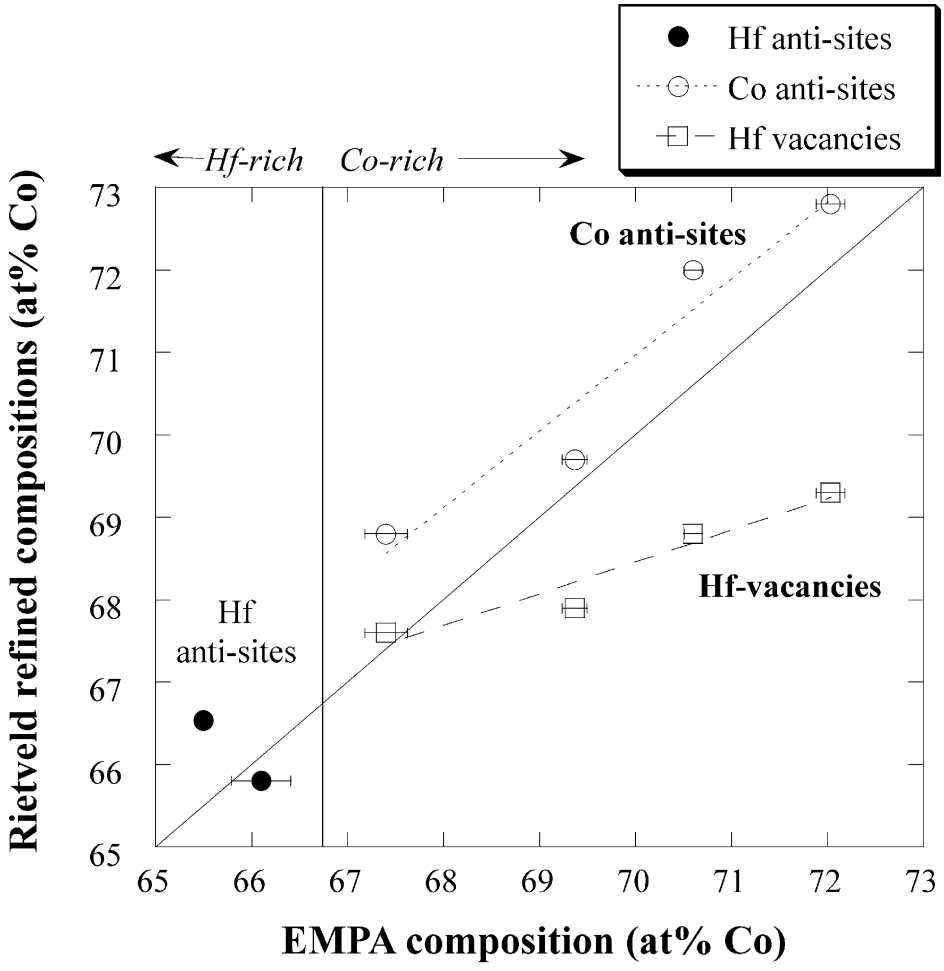

Fig. 8. Rietveld refined compositions based on different defect mechanisms compared against the microprobe compositions.

anti-sites has a slope close to 1, but off-set to compositions roughly 1 at.% greater than the microprobe compositions. The refined compositions with Hf-vacancies match the Hf–67.4 Co alloy, but then deviate further away with increasing off-stoichiometry. The slope (or compositional dependence) does not represent a good fit. Thus, Co anti-sites for the Co-rich $HfCo_2$ compositions appear to be the dominant defect mechanism.

On the other hand, refinements on the atomic contents for the Hf-rich $HfCo_2$ alloys are less successful. When the Co-sublattice sites are refined to allow vacancies, the occupancy converges to a nonsensical value of greater than one. Refinements with Hf anti-sites are possible, but give the wrong trend in Fig. 8. More samples on the Hf-rich side of stoichiometry would be preferable to utilize this technique, and instead, other methods will be used to elucidate the defect mechanism for Hf-rich $HfCo_2$ Laves phases.

3.4. Density

The densities of the single-phase *C*15 samples are plotted in Fig. 9 as a function of Laves phase composition. A steady decrease in density occurs with an increase in the Co-content of $HfCo_2$. Calculated densities of the alloys with the two possible defect types are also plotted. The calculated densities assume a particular defect mechanism (Table 2) in order to determine the constituents of the unit cell. The experimental volume (from XRD lattice constants) for a particular composition is used to compute the density, and a smoothing curve is generated.

The calculated densities of alloys with vacancies quickly decrease with deviation from stoichiometry, as to be expected with the absence of atoms. Calculated densities of alloys with anti-site substitutions, however, show a very different trend. Hf-rich Laves compositions display greater densities than the stoichiometric composition, while the densities of Co-rich compositions gradually decrease in value. The experimental data follow the trend of the calculated densities of alloys with anti-site substitutions quite well, although the experimental values are roughly 2% below the calculated values.

4. Discussion

4.1. $HfCo_2$ Laves phase field

The phase stability of a Laves phase (AB_2) is often attributed to size effects, and the ideal radius ratio of the A and B atoms is given as $R_A/R_B = 1.225$. However,

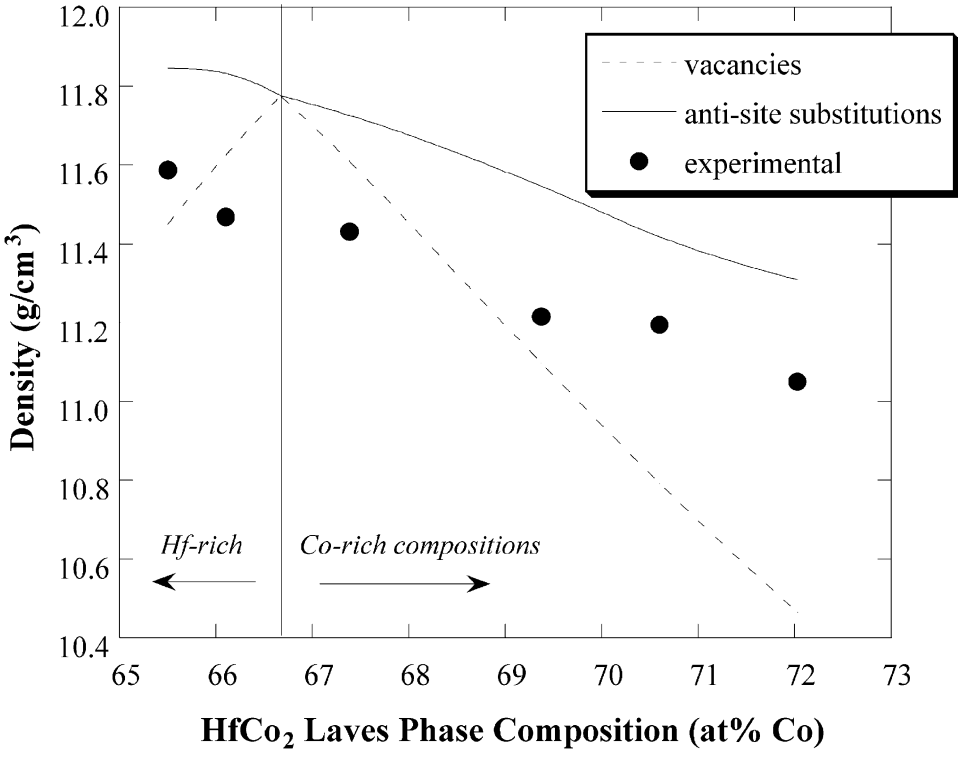

Fig. 9. Densities of the single-phase $HfCo_2$ Laves phases. Calculated densities of compositions with the anti-site substitution and with the vacancy defect mechanism are also plotted.

Laves phases exist with radius ratios from 1.05 to 1.68, and electronic contributions also play a role in the phase stability [26]. Nevertheless, atomic sizes are a consequence of the electronic structure and provide a convenient method to geometrically model Laves phase solubility limits.

The ideal size ratio allows for the greatest possible packing efficiency of 0.71 for a topologically close-packed structure (and assuming a hard sphere model). The atomic size ratio has been used to correlate Laves phases with their solubility limits. Out of the known 360 binary Laves phases, only 25% have a defined solubility and less than 20% have ranges greater than 2 at.%. The Laves phases which do report solubility ranges have radius ratios close to the ideal value. For example, the *C*15 phases that exhibit solubility have radius ratios between 1.1 and 1.35. Such a correlation can be understood in terms of lattice-adjusted contractions. As the radius ratio departs from the ideal value, specific sublattice contractions or expansions must occur to achieve the optimal packing efficiency, and thus solubility limits are affected [4].

Such size arguments are insightful to understand the solubility range of $HfCo_2$. Using the metallic atomic radii (CN12), $R_{Hf} = 1.58$ Å and $R_{Co} = 1.25$ Å [27], the radius ratio of $HfCo_2$ is 1.264, and is fairly close to the ideal value. Accordingly, a relatively large solubility range exists for $HfCo_2$. Also, the radius ratio for $HfCo_2$ is larger than the ideal value, and correlates with a more pronounced solubility on the B-rich side of stoichiometry. By geometrical requirements, a smaller B atom would substitute onto the A-sublattice more easily than the larger A atom onto the B-sublattice (if anti-site substitutions are operative). The solubility range on the B-rich side (5.3 at.%) of $HfCo_2$ is at least 3 times larger than the solubility range on the A-rich side (1.7 at.%).

In the Laves phase structure, the A atom has 12 B atoms as its nearest neighbor, and the B atom is surrounded by six A atoms. As anti-site defects are incorporated into the lattice, the immediate environment for an atom becomes more rich in either A or B atoms. Taken to the extreme, the local environment can resemble the pure metal form. Thus, the effective size of the atoms may vary between the predicted size in the Laves phase, r, and the elemental metallic size, R.

The atomic sizes in the Laves phase (r) is computed from the geometry of the idealized Laves structure (Fig. 10) and the extrapolated stoichiometric lattice constant ($a_0 = 6.9002$ Å).

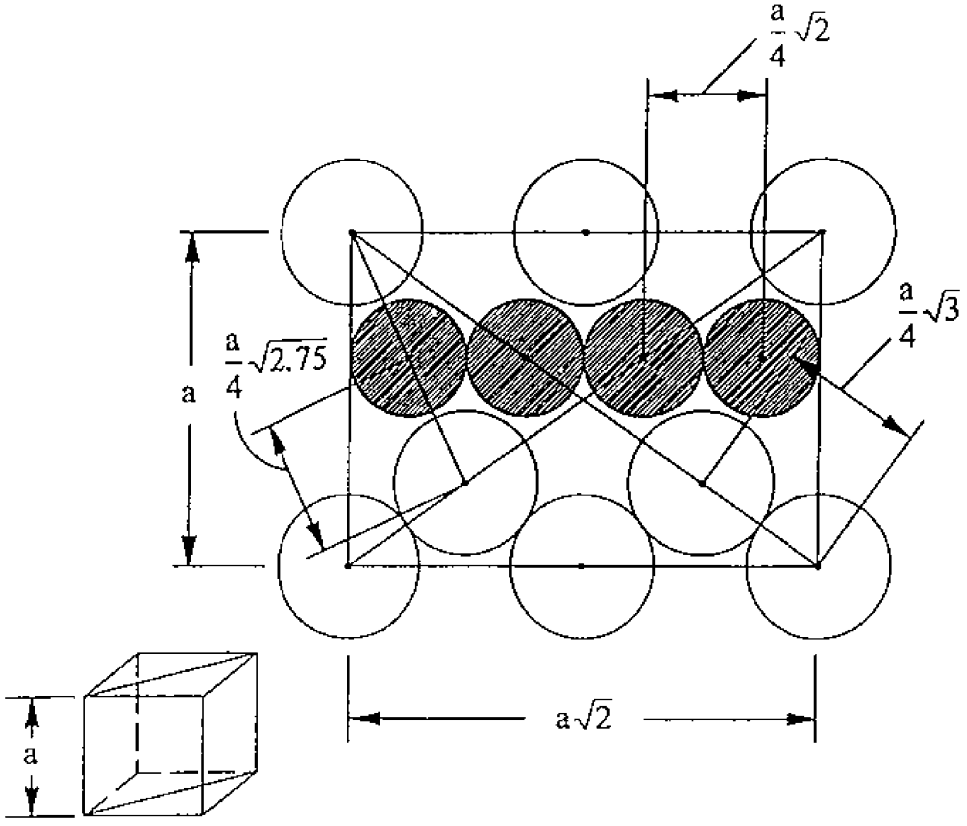

Fig. 10. Schematic diagram of the (110) plane in the *C*15 Laves structure illustrating the distances of the A atoms (large open circles) and B atoms (small hatched circles) in terms of the lattice constant.

$$r_A = \sqrt{3/8}a_0 \tag{4}$$

$$r_B = \sqrt{2/8}a_0 \tag{5}$$

The values for r_{Hf} and r_{Co} are then used to compute an "average" atomic size (r_{ave}) for a particular alloy composition from the weighted-average of the two radii. Thus Vegard's Rule is employed in the following equation (where x is the at.% of the B atom, or Co):

$$r_{ave} = (1 - x)r_A + xr_B \tag{6}$$

This average radius value is then used to compute the $C15$ lattice constant based on the atomic packing of the structure. The $C15$ lattice constant (a) is computed from the following equations where the 24 atoms of r_{ave} comprise 71% of the total unit cell volume:

$$0.71 \times a_r^3 = 24 \times 4/3\pi r_{ave}^3 \tag{7}$$

a_r represents the lattice constant using radii of atoms in the intermetallic form [from Eqs. (4) and (5)], and is only a geometrical construct that assumes a single sized atom (r_{ave}). The true Laves structure of two dissimilar atoms is not represented. Nonetheless, the lattice constant, a_r, becomes a function of composition through Eqs. (6) and (7).

Likewise, the same geometrical constructs are developed using the elemental atomic sizes, R.

$$R_{ave} = (1 - x)R_A + xR_B \tag{8}$$

$$0.71 \times a_R^3 = 24 \times 4/3\pi R_{ave}^3 \tag{9}$$

Now, a_R represents the lattice constant of a $C15$ structure with atom sizes of the elemental form (R). The two expressions for the lattice constant (a_r and a_R) as a function of composition become boundaries to the solubility limits for the Laves phase, and are constructed in Fig. 11.

Since the geometric models and constructs are based upon atomic substitutions (e.g. Vegard's Rule), the constructed solubility limits represent anti-site substitutions. The experimental lattice constants of the different $HfCo_2$ samples are plotted in Fig. 11, and fall within the boundary limits. Thus, the anti-site substitution defect mechanism in $HfCo_2$ is feasible. In turn, these geometrical constructs can also be used to predict the possible solubility range of Laves phases.

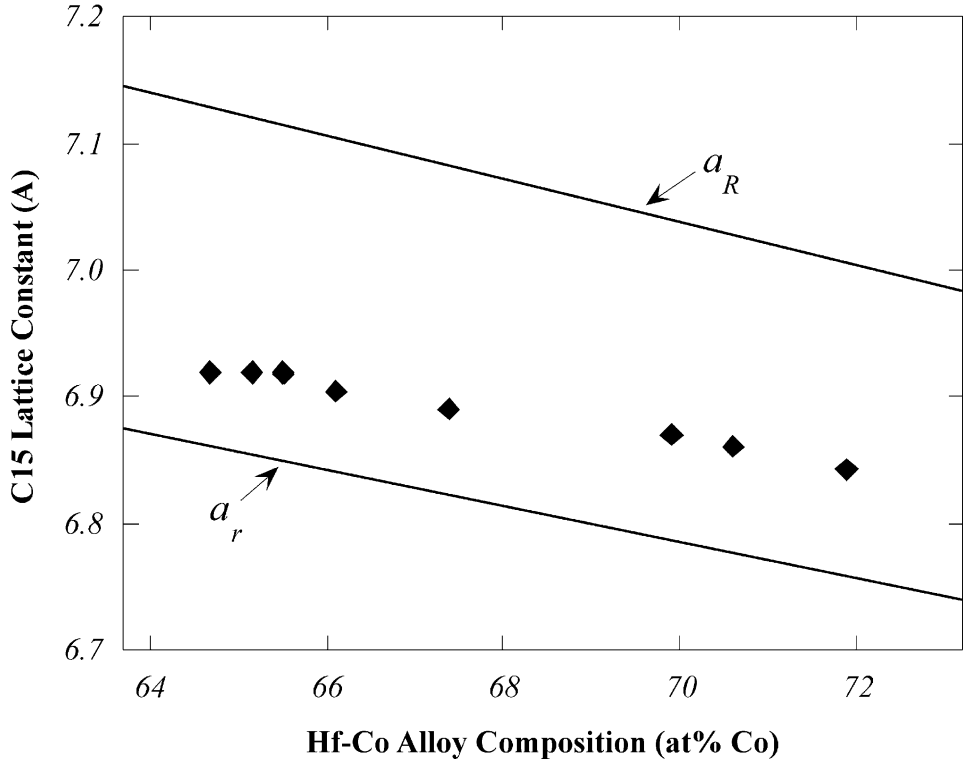

Fig. 11. Experimentally determined $C15$ lattice constants are bounded by limits determined by expressions for a_r and a_R as a function of composition [Eqs. (7) and (9)].

4.2. Defect mechanism

A fairly linear dependence of the Laves phase lattice constant on the alloy composition occurs within the $HfCo_2$ phase field (Fig. 5), suggesting that the same defect mechanism is operative on both sides of the $HfCo_2$ stoichiometry. A distinct break in slope at stoichiometry is not evident as in the cases of the $NbCr_2$ [7] and YAl_2 [17] Laves phases. Different defect mechanisms were suggested as the cause for the discontinuity in slope near stoichiometric $NbCr_2$ and AlY_2, however later studies have demonstrated anti-site substitution on both sides of stoichiometry [8].

As the Laves compositions become increasingly Hf-rich, the *C*15 lattice constants increase. Since Hf atoms are larger than the Co atoms, excess Hf atoms on the Co-sublattice are expected to increase the lattice constant. Likewise, excess Co in Co-rich $HfCo_2$ compositions would decrease the lattice constant, and the experimental results concur. The effect of constitutional vacancies on Laves phase lattice constants has not been conclusively established, but other experimental techniques (e.g. density, Rietveld refinements) indicate that vacancies are not the dominant defect mechanism.

The strain parameters from the Rietveld refinements display interesting trends in Fig. 6. The strain parallel to [111] is along the direction for stacking of the close-packed planes, while the strain perpendicular to [111] involves strain within the close-packed planes. Differences between the two strain values demonstrate the degree of strain anisotropy in the material. The increase in strain within the (111) planes is expected with anti-site substitutions as the compositions deviate from stoichiometry. As the compositions become more Hf- or Co-rich, the anisotropy increases demonstrably, and signifies the departure from a "perfect" crystalline lattice.

The Laves compositions greater than 70 at.% Co are disregarded since these compositions have an additional influence of the onset of magnetism. $ZrMn_2$, has also been reported to have a minimum in the half-widths of XRD peaks (i.e. strain) at stoichiometry [28]. Excess Mn was determined to occupy the A-sublattice of the *C*14 $ZrMn_2$ Laves phase by Rietveld refinements.

Annealing of the powder samples result in a small decrease in strain, and indicate that preparation of the powders may produce residual strains in the samples and deformation may have been induced during the grinding steps. The curious trend of the Hf-rich alloys after annealing is not well understood. However, the increased anisotropy in strain with nonstoichiometry remains even after annealing.

The experimental XRD intensities do not match the simulations perfectly, but comparisons between the two defect models lend credence towards the anti-site mechanism (Fig. 7). Likewise, the trends of the Rietveld-refined compositions with anti-site substitution on the Co-rich side of stoichiometry appear to have the best fit with the microprobe data (Fig. 8). These two methods rely on the XRD intensities, and thus, should have similar conclusions. The Rietveld refinement techniques and XRD simulations are new and additional experimental methods to identify defects in Laves phases, and suggest that the defect structures are more complicated than the models of solely random anti-sites or vacancies in the lattice. Ordering of defects or combinations of defect types would affect the XRD intensities, and are not taken into account in this study.

The trend of the experimental densities versus the Laves phase composition follows that of the calculated densities with anti-site substituted alloys (Fig. 9). Although the experimental density values do not match the calculated values exactly, such discrepancies can be easily attributed to microcracks or voids in the samples. Since monolithic Laves phases are very brittle, microcracks can be formed during processing. The measured density for $TiMn_2$ was also found to be lower than the calculated value, and is attributed to internal cracks [15]. Likewise, the densities of the $TiCr_2$ Laves phase appear to follow the calculated anti-site substituted alloy densities and also have lower values (about 1%) than the calculated values [6]. Furthermore, on the Hf-rich side of stoichiometry, the calculated vacancy densities drop rapidly while the anti-site density increases. The experimental density values increase for the Hf-rich Laves phases, and conclusively indicates anti-site substitutions as the dominant defect mechanism.

In addition, other investigators [23,29] report increases in the magnetic susceptibility with Co-rich $HfCo_2$ Laves phases. Such an effect is believed to be due to the magnetic moment of excess Co in the Laves phase, and is consistent with anti-site substitutions.

Thus, significant evidence from several different approaches (i.e. trends in lattice constants, density, XRD intensities and peak widths, geometrical modeling) suggest that the nonstoichiometry in $HfCo_2$ Laves phases is predominately accommodated by anti-site substitutions.

4.3. Deformation

The identification of defects in Laves phases is fundamental to the understanding of deformability and mechanical properties. Many Laves phases exhibit severe brittleness, and deformation can only be improved with knowledge of structure-property relationships. Deformation of Laves phases is currently understood in terms of the "synchroshear" process, whereby consecutive layers of A atoms and B atoms move in a coordinated and synchronous manner [30]. Anti-site atoms or vacancies (i.e. lack of atoms) can act as impedance or facilitators to this process of atomic motions. The passage of partial dislocations requires

that atoms exchange positions, and vacancies are thought to aid in the process [31]. In addition, anti-site substitutions or alloying additions that produce greater "open volume" in the lattice are thought to facilitate atomic motions involved in the synchroshear deformation process [32,33]. Strain along the direction of stacking of the close-packed planes is seen to decrease with off-stoichiometry (Fig. 6). Defects associated with non-stoichiometric Laves phase compositions will therefore have an impact on the synchroshear mechanism and deformation behavior.

The implication that defects affect mechanical properties has been substantiated with hardness and fracture toughness measurements in $TiCr_2$ Laves phase alloys [34]. Off-stoichiometric Laves compositions are associated with improved toughness. Thus, extending or identifying large solubility limits are strategies to improve the brittle tendencies of Laves phases. Furthermore, alloying additions can extend the Laves phase fields, especially when moving into ternary space. Thus, alloying becomes another toughening scheme and will be pursued with future studies.

This effect of anti-site substitution defects on the mechanical properties in $HfCo_2$ Laves phases is investigated in Part II of this study.

5. Conclusions

Several techniques are employed to identify anti-site substitutions as the dominant defect mechanism in the $HfCo_2$ binary Laves phase intermetallic, and the results are enumerated below.

1. The solubility limits of the $C15$ $HfCo_2$ Laves intermetallic has been determined by metallography, electron probe microanalysis (EPMA), and X-ray diffraction (XRD) to extent from 65.0 at.% Co to at least 72.0 at.% Co.
2. Within the single-phase field, the $C15$ $HfCo_2$ lattice constants (a) vary from 6.9190 Å (Hf-rich) to 6.8427 Å (Co-rich), with an almost linear relationship with composition (x = at.% Co): $a = 7.6409 - 0.011107x$. An anti-site substitution mechanism is consistent with such a trend.
3. Rietveld refinements on XRD scans are used to determine the strain $\parallel$ [111] and the strain $\perp$ [111]. Increased strains within the close-packed planes as compositions deviate from stoichiometry are consistent with the anti-site substitutions. Anisotropy in the strains are also evident with nonstoichiometric compositions.
4. Experimental XRD intensities are most consistent with simulated XRD scans and with Rietveld-refined alloy compositions for alloy compositions based on an anti-site substitution model.
5. Compositional trends of the experimental density of $HfCo_2$ follow the trends of calculated density values for alloys with anti-site substitutions.
6. Anti-site substitutions are consistent with the geometrical models used to calculate boundaries for the solubility range of $HfCo_2$.

Acknowledgements

The electron microprobe work was performed by William Hutchinson at LANL. This research has been supported by the Office of Basic Energy Sciences, Department of Energy.

References

[1] Livingston JD. Phys Stat Sol (a) 1992;131:415.
[2] Clark AE. In: Wohlfarth EP, editor. Ferromagnetic materials, vol. I. Amsterdam, North-Holland. 1980, p. 531.
[3] Ivey D, Northwood D. J Less-Common Metals 1986;115:23.
[4] Thoma DJ, Perepezko JH. J Alloys and Compounds 1995; 224:330.
[5] Ishida K, Nishizawa T. In: Massalaski TB, editor. Binary alloy phase diagrams, 2nd ed. Materials Park, (OH): ASM, 1990. p. 1194.
[6] Chen KC, Allen SM, Livingston JD. In: High-temperature ordered intermetallic alloys VI. MRS Symp Proc 1994;364: 1401.
[7] 5Thoma DJ, Perepezko JH. Mater Sci Eng A 1992;156:97.
[8] Zhu JH, Pike LM, Liu CT, Liaw PK. Acta Mater 1999;47:2003.
[9] Zhu JH, Pike LM, Liaw PK, Liu CT. Scripta Mater 1998; 39:833.
[10] Zhu JH, Liu CT. Acta Mater 2000;48:2339.
[11] Saito S, Beck PA. Trans AIME 1960;218:670.
[12] Pargeter JK, Hume-Rothery W. J Less-Common Metals 1967; 12:366.
[13] Smith AW, Rogers JA, Rawlings RD. Phys Stat Sol (a) 1973; 15:K119.
[14] Bruckner W, Perthel R, Kleinstuck K, Schulze GER. Phys Stat Sol 1968;29:211.
[15] Waterstrat RM, Das BN, Beck PA. Trans AIME 1962;224: 512.
[16] Sinha VK, Wallace WE. J Less-Common Metals 1985;106:199.
[17] Foley JC, Thoma DJ, Perepezko JH. Metall Mater Trans A 1994; 25:230.
[18] Livingston JD, Hall EL. J Mater Res 1990;5:5.
[19] Westbrook JH. In: Westbrook JH, editor. Mechanical properties of intermetallic compounds. John Wiley & Sons, 1960.
[20] Chen KC, Chu F, Kotula PG, Thoma DJ. Part II of paper. This issue.
[21] Rietveld HM. J Appl Crystallogr 1969;2:65.
[22] Larson AC, Von Dreele RB. In: GSAS, General structural analysis system, Document LAUR 86-748. Los Alamos (NM): Los Alamos National Laboratory, 1993.
[23] Peterson EJ. Work in progress.
[24] Pennings ECM, Grellner W. J Am Ceram Soc 1989;72:1268.
[25] Zimmerman C, Perepezko JH, Matyi RJ, Thoma DJ. Work in progress.
[26] Laves F, Witte H. Metallwertschaft 1936;15:840.

[27] Pearson WB. In: Crystal chemistry and physics of metals and alloys. Wiley, 1972.
[28] Kodama T, Anada H, Kaminaka H. J Alloys and Compounds 1995;224:70.
[29] Aoki Y, Nakamichi T, Yamamoto M. Phys Stat Sol (b) 1973; 56:K17.
[30] Amelinckx S. In: Nabarro FRN, editor. Dislocations in solids, vol. 2. Amsterdam: North-Holland, 1979. p. 67.
[31] Hazzledine PM, Kumar KS, Miracle DB, Jackson AG. In: High-temperature ordered intermetallic alloys V. MRS Symp Proc 1992;288:591.
[32] Chu F, Pope DP. Mat Sci and Eng A 1993;170:39.
[33] Takasugi T, Yoshida M, Hanada S. Acta Mater 1996;44:669.
[34] Chen KC, Allen SM, Livingston JD. Mater Sci Eng A 1997;239–240:251.